

BOOSTING EFFICIENCY UP TO 34.5% OF CIGS-BASED SOLAR CELLS USING A NEW HETEROSTRUCTURE BY SIMULATION

MOHAMED MOUSTAFA^{1,*}, SHADI YASIN², MOHAMED SWILLAM¹

¹ Department of Physics, School of Sciences and Engineering, The American University in Cairo, AUC Avenue, P.O. Box 74, New Cairo 11835, Egypt

E-mails: mohamed.orabi@aucegypt.edu; m.swillam@aucegypt.edu

² Physics Program, Department of Mathematics, Statistics, and Physics, College of Arts and Sciences, Qatar University, P.O. 2713, Doha, Qatar

E-mail: syasin@qu.edu.qa

* *Corresponding author:* mohamed.orabi@aucegypt.edu

Received April 24, 2023

Abstract. This work explores the photovoltaic performance of a high efficiency heterostructure based on CIGS solar cells using SCAPS. Various electrical specifications were explored at various thicknesses and doping densities. Initially, photovoltaic characteristics of the ITO/GaSe/CIGS heterostructure are investigated. The results show an optimized PCE of 22.59%. Then, a thin film strongly doped *p*-type is employed (CIGS-*p*⁺) to the structure. The engagement of the CIGS-*p*⁺ layer increases the PCE to 31.94%. The proposed CIGS-*p*⁺ layer is interpreted to serve as a back surface field. The structure is further improved by adding a third interfacial layer of *p*-MoS₂ transition metal dichalcogenide material between the absorber and the Mo back contact. Adding a third interfacial layer implied an efficiency increase of 34.55%. The results reveal that the MoS₂ layer at the CIGS/Mo interface adapts it creating Schottky-type contact to quasi-ohmic contact. The results confirm the beneficial influence of the interface layers on the CIGS heterostructure. Additionally, the performance of the photovoltaic cell against the defect intensity of the absorber layers is found to degrade behind a level of $1 \times 10^{18} \text{ cm}^{-3}$. An ITO/GaSe/CIGS/CIGS-*p*⁺ based structure exhibited the highest stability in performance against the temperature change among the three examined systems.

Key words: SCAPS simulation, CIGS, CIGS-*p*⁺, TFSCs, defect density.

DOI: <https://doi.org/10.59277/RomJPhys.2023.68.621>

1. INTRODUCTION

Since the world's population is continuously increasing, energy demand also increases. Accordingly, a dramatic increase in the utilization and development of renewable energy resources and technologies is undoubtedly needed. Solar energy is a promising source since it is a green, abundant, sustainable, and natural source as long as the Sun exists. Therefore, it is of considerable research to explore materials that, on the one side, are optimal for energy conversion and, on the other side, esteem the surroundings. Extensive efforts and research are devoted to solar energy and photovoltaic (PV) technologies. Nevertheless, above 75% of PV production is based on Si wafer technologies [1]. In recent years, thin-film solar cells (TFSC) for PV applications have received significant consideration due to their remarkable characteristics

and performances. Research demands several aspects to enhance cell stability and performance, cost scaling down, and minimize environmental impact. Amongst them, Cu(In, Ga)Se₂, the CIGS, has received significant consideration as one of the potential candidates for high-efficiency TFSC applications [2–5]. CIGS possesses many advantages due to their physical and electrical properties. In CIGS-based solar cells. The bandgap (E_g) values vary over the spectrum from 1.0 eV to 1.7 eV and can be tailored by changing the fraction molar (x) parameter in CuIn _{x} Ga_{1- x} S general formula [6–8]. Additionally, CIGS has an excellent absorption coefficient of around 10^5 cm^{-1} , with high exterior stability [9]. High efficiencies of 20.3% and 22% for a laboratory-scale CIGS solar cell have been reported [3, 9]. The power conversion efficiency of 17.4% for the CIGS thin-film structure is achieved [10], and about 19.9% has been completed for solar cells using CIGS [11].

Although the CIGS has now been a supreme absorber material for TFSC, optimizing the buffer layer is a debatable and necessary step toward improving solar cell performance [12]. The most frequently applied buffer layer is the CdS. Nevertheless, the demerits of CdS cannot be ignored. Cd element is a highly toxic material. Disposal of the Cd-containing outputs causes a damaging consequence on human well-being, and suitable treatment of a large amount of poisonous waste might be a very challenging and costly task. Aside from the toxic feature of the CdS, it possesses a band gap of 2.4 eV to 2.5 eV, which implies a severe optical absorption drop in the short wavelength spectrum, limiting the overall performance of solar cells. Due to some disadvantageous properties of CdS as a buffer layer, many efforts and investigations have been put into finding Cd-free alternative buffer candidates, for example, Zn(O, S, OH), ZnS, ZnSe, Zn(O, OH), ZrO and InS [13–16]. The article proposes a new CIGS-based solar cell structure using Gallium Selenide (GaSe) as a novel buffer layer and an ITO anti-reflective film. GaSe is a III–VI semiconductor with a layered structure in which the essential element is a sheet. It comprises two Ga planes interspersed between two Se planes with a Se–Ga–Ga–Se sequence [17]. Strong bonds between atoms exist inside the same sheet, while all the sheets constituting the 2D lamellar crystal are tied by weak Van-der-Walls type bonds [18, 19]. All these polytypes are broadband semiconductors with around 2.00 eV [20] and 2.16 eV [21] values. Accordingly, the low dimensional layered materials GaSe has received much attention for buffer layer implementations.

Molybdenum (Mo) is an extensively used material for back contact for CIGS-based solar cells. The material reported 4.6 eV of work function. CIGS solar cells employing various back-contact materials and discussed that Molybdenum and Tungsten contacts deliver the greatest CIGS/back contact interface passivation has been reported by Orgassa *et al.* [22]. Moreover, it has been revealed that Mo back contacts form a Schottky-type barrier with the CuInSe₂ absorber [23, 24]. On the other hand, it was found that the forming suitable intermediate layer between the CIGS absorber and Mo in the CIGS deposition secures low resistance quasi-ohmic contact on replacing back contact materials [25, 26]. Using this style, the contact between Mo and CIGS revealed an ohmic contact type [27]. This paper concerns the MoS₂ interfacial layer of

group VI of the layered transition metal dichalcogenides group (TMDCs). The TMDC materials show outstanding structural properties because of their remarkable 2D character. Their structure consists of an X-M-X atomic layer where a sheet of metal atoms is sandwiched between two chalcogen sheets and weak van der Waals forces hold sheets together [28]. The TMDCs are characterized by their chemical and thermal stabilities of the *n*- and *p*-type character correlated with high carrier mobilities.

Using the SCAPS software, this paper studies a new CIGS-based solar cell structure with a GaSe buffer layer and an ITO film. Initially, for the ITO/GaSe/CIGS heterostructure, the performance parameters of the solar cell, the open circuit voltage V_{oc} , short circuit current density J_{sc} , Fill Factor FF, and the power conversion efficiency PCE are investigated *versus* the absorber thickness and the doping concentration. Then, to improve the solar cell's efficiency, a CIGS- p^+ is added to lower the charge carrier losses at the back face. Thirdly, a *p*-MoS₂ transition metal dichalcogenide (TMDC) layer is added as an interfacial layer between the CIGS/CIGS- p^+ absorber and Mo back contact, *i.e.*, ITO/GaSe/CIGS/CIGS- p^+ /*p*-MoS₂ structure. The effect of *p*-MoS₂ (TMDC) as an interfacial layer on solar cell performance is interpreted. The presence of defects strongly affects the optical and optical parameters of semiconductor materials. As such, defect study is vital for improving the output characteristics of photovoltaic cells. Following the optimization of cell thickness excluding the defects state, the photovoltaic parameters considering the defects in the region of each active absorber layer have been discussed. Indeed, the overall performance of TFSCs is affected under high-ambient temperature conditions. The practical results revealed that all electrical parameters of the solar cells have changed with temperature variation [29]. Eventually, the effect of the temperature on the device's performance, from 300 K to 500 K, is presented and discussed.

2. NUMERICAL SIMULATION AND MATERIAL PARAMETERS

This work tracks the impact of intrinsic and extrinsic parameters, such as defect states and temperature, on the photovoltaics performance of CIGS-TFSCs by utilizing the SCAPS-1D solar cell simulation package [30, 31]. SCAPS has been proven powerful simulation software for simulating and predicting the performance of several solar cells, for example, Perovskite, CZTS, CZTSe, CdTe, and organic and polymeric solar cells [32–35]. It offers advantages such as the analyses of heterojunction and multi-junction photovoltaic devices. Additionally, the simulation outcomes correspond well with previous practical and experimental work producers, encouraging the researcher to use it as a reliable simulation. SCAPS can be operated under different AC and DC testing conditions. Also, it can describe solar cell structures up to seven layers with various characteristics, input materials, and device parameters such as layer thickness, energy bandgap, electron affinity, defect, and doping densities. Here, the simulations are carried out under standard testing states of AM 1.5 electromagnetic spectrum, a 1000 W/m² light intensity, and an operating temperature of 298 K.

Figure 1 shows the schematic configuration of the employed CIGS solar cell structure. A typical CIGS-based solar cell structure consists of a p -type wide-bandgap absorber layer deposited on the Molybdenum (Mo) coated back glass substrate. A buffer layer n -type and window layer. Structure 1 consists of ITO/GaSe/CIGS structure using GaSe as a buffer layer. Then, for structures 2 and 3, a layer of CIGS- p^+ is added, and an additional p - MoS_2 as an interfacial layer is added, respectively, to enhance the overall performance of the solar cell. The structure is initiated with the soda-lime glass substrate. The MoS_2 is a layered semiconductor that can exist in both n - and p -type with a net carrier concentration of about 10^{18} cm^{-3} and Hall mobilities of $\sim 155 \text{ cm}^2/\text{Vs}$ at 298 K. The various materials properties embedded in the current simulation are listed in Table 1, after Refs. [36–38]. Indeed, simulation in SCAPS mainly focuses on mapping the energy diagrams in steady states by solving three coupled semiconductor equations: Poisson's equation, and the continuity equation for electrons and holes (equations 1–3). These coupled equations in the software calculate the electron-hole recombination profile with the charge carriers transport in one dimension

$$\frac{\partial}{\partial x} \left(\epsilon_0 \epsilon_r \frac{\partial \Psi}{\partial x} \right) = -q(p - n + N_D^+ - N_A^- + \frac{\rho}{q}) \quad (1)$$

$$-\left(\frac{1}{q}\right) \frac{\partial J_n}{\partial x} - U_n + G = \frac{\partial n}{\partial t} \quad (2)$$

$$-\left(\frac{1}{q}\right) \frac{\partial J_p}{\partial x} - U_p + G = \frac{\partial p}{\partial t}, \quad (3)$$

where Ψ and ρ are the electrostatic potential function and the defects charge density, respectively. n and p are the free carrier concentrations whereas N_A^- and N_D^+ are the densities of ionized acceptors and donors, ϵ_0 is the absolute permittivity while ϵ_r is the relative permittivity of the material, respectively. G , J_p and J_n are the generation rate, the hole, and electron current densities.

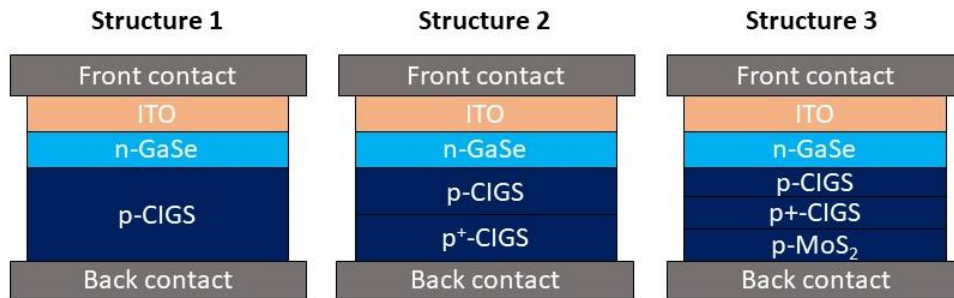


Fig. 1 – Structure 1 represents the CIGS solar cell ITO/GaSe/CIGS structure using GaSe as a buffer layer. For structure 2, a layer of CIGS- p^+ is added, and for structure 3, an additional MoS_2 as an interfacial layer is added.

Table 1

Important parameters and constants of materials utilized in simulating all structures

Parameters	ITO	n-GaSe	p-CIGS	p ⁺ -CIGS	MoS ₂
Thickness (nm)	300	100	300	300	500
Band gap (eV)	3.6	2.2	1.4	1.4	1.4
Electron affinity (eV)	4.5	4.5	4.5	4.5	4.2
Dielectric-permittivity	8.9	8	13.6	13.6	11.9
CB effective density of states (cm ⁻³)	2.2×10^{18}	1.4×10^{18}	2.2×10^{18}	2.2×10^{18}	7.5×10^{17}
VB effective density of states (cm ⁻³)	1.8×10^{19}	1.49×10^{19}	1.8×10^{19}	1.8×10^{19}	1.8×10^{18}
Electron thermal velocity (cm/s)	1×10^7	1×10^7	1×10^7	1×10^7	1×10^7
Hole thermal velocity (cm/s)	1×10^7	1×10^7	1×10^7	1×10^7	1×10^7
Electron mobility (cm ² /Vs)	10	250	100	100	100
Hole mobility (cm ² /Vs)	10	25	25	25	150
Donor doping concentration (cm ⁻³)	1×10^{18}	1×10^{18}	0	0	0
Acceptor doping concentration (cm ⁻³)	0	0	1×10^{17}	1×10^{21}	1×10^{17}

3. RESULTS AND DISCUSSIONS

The thickness of the absorber layer parameter is essential in identifying the efficiency of the solar cell and in reducing the overall cost of the production of the device. Along with this direction, the simulation was performed to investigate the cell performance *versus* the CIGS absorber thickness. Figure 2a–d depicts the extracted solar cell performance parameters of the ITO/GaSe/CIGS structure. The thickness was varied from 100 nm to 1000 nm. The results show that the performance is enhanced by increasing the thickness of the absorber layer. The deduced results of the cell parameters for different thicknesses of the CIGS absorber layer are collected in Table 2. It is noted that the J_{sc} enhances with the increase of the thickness of the absorber layer, so the efficiency improves. For instance, the J_{sc} increases from ~ 22.7 mA/cm² to ~ 28.6 mA/cm², with the thickness going from 200 nm to 1000 nm. An optimum efficiency reaches $\sim 22.6\%$ and is obtained at the CIGS thickness at 1000 nm. The solar cell estimated current-voltage (J – V) characteristics of the solar cell performance are depicted in Fig. 2e using input parameters for three different thicknesses. Figure 2f represents the change in quantum efficiency (QE) against the wavelength. The QE probe the correlation between the bandgap values and the carrier collection. It can be noticed that the obtained QE improves with increasing the absorber thickness, a behavior that matches well with prior work, *e.g.* [5]. The optimized parameters of the ITO/GaSe/CIGS structure are the V_{oc} of 0.93 V, J_{sc} of 28.40 mA/cm², FF of 85.12%, and PCE of 22.59%. The obtained results can be discussed considering the back contact recombination current density and its

correlations with the absorber thickness. As previously reported, decreasing the thickness of the absorber layer in TFSC reveals J_{sc} and V_{oc} to reduce. The back contact is established for the thin absorber layer close to the depletion region. In these cases, a part of the incoming lower energy photons is absorbed nearer to the back contact. As such, a percentage of the photogenerated carriers will recombine at the back contact, and this mechanism can be prevented by enhancing the thickness of the absorber layer.

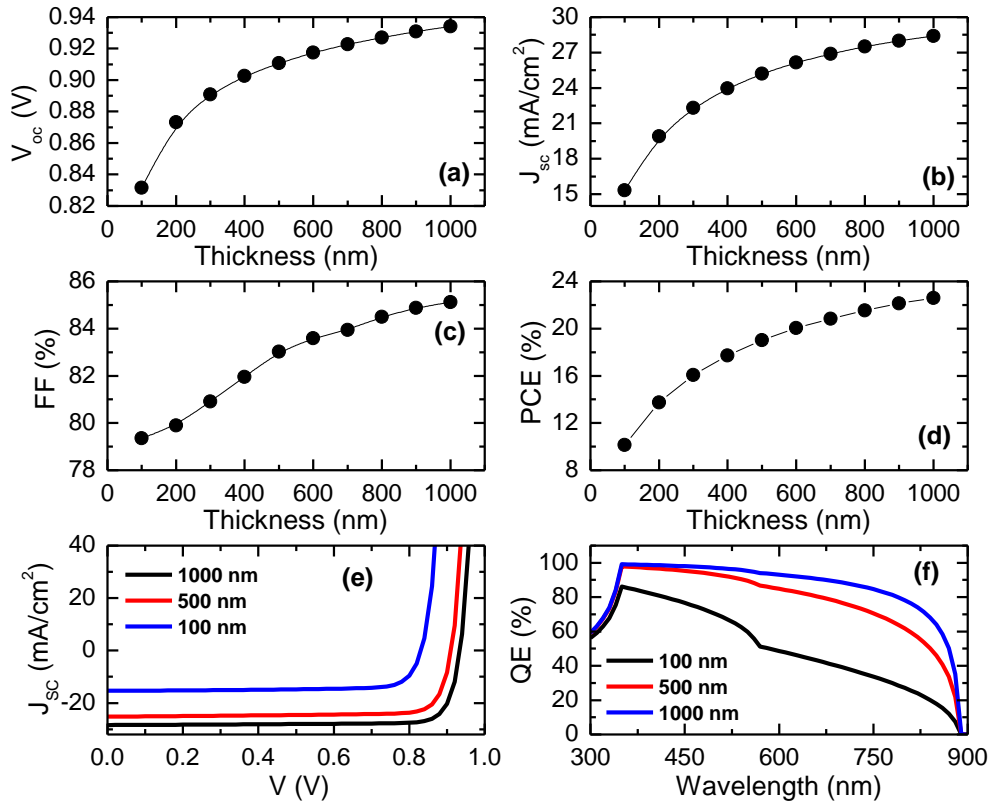


Fig. 2 – a–d (Online Color) Effect of the *p*-CIGS absorber layer thickness in ITO/GaSe/CIGS structure on the solar cell specifications; e) J - V at different absorber layer thicknesses; f) the obtained simulated external quantum efficiency EQE.

The effect of the carrier (doping) concentration of the absorber layer on the solar cell performance parameters is discussed in Fig. 3. The doping concentration was changed from $1 \times 10^{13} \text{ cm}^{-3}$ to $1 \times 10^{22} \text{ cm}^{-3}$. As observed in Fig. 3, the carrier concentration of the CIGS absorber significantly affects the device's performance. Figure 3b shows the obtained relationship between the J_{sc} and the absorber layer

carrier concentration. The J_{sc} is observed to increase with the carrier concentration. The observed trend might be due to reducing the lifetime of the photogenerated electrons associated with the increase of the carrier concentration, which reduces the possibilities of carrier collection and, as such, lower J_{sc} . Further, increasing the carrier concentration from $1 \times 10^{13} \text{ cm}^{-3}$ to $1 \times 10^{22} \text{ cm}^{-3}$ resulted in an increment in the V_{oc} , FF, and PCE. The V_{oc} values can be calculated using equation (4). Increasing the absorber carrier concentration will cause a reduction in the reverse saturation current J_o , an increment in the parameter V_{oc} following the equation below,

$$V_{oc} = \frac{nkT}{q} \ln\left(\frac{J_{ph}}{J_o} + 1\right), \quad (4)$$

where J_{ph} and J_o are the photogenerated and the reverse saturation current densities, respectively. n is the ideality factor, k is the Boltzmann's constant, and T is the absolute temperature. The PCE of a solar cell is related to the J_{sc} , and the V_{oc} using the FF according to equation (5):

$$\text{PCE} = \frac{V_{oc} J_{sc} \text{FF}}{P_{in}} \quad (5)$$

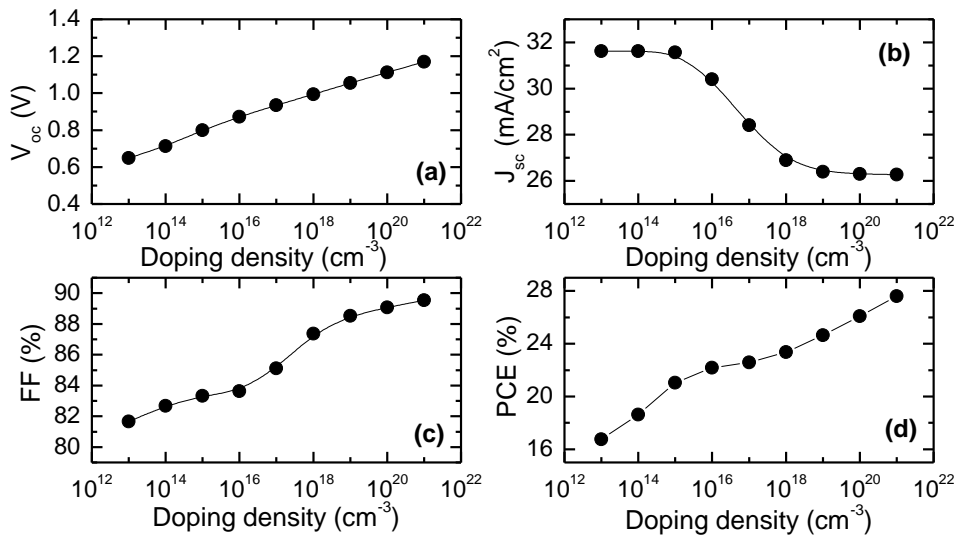


Fig. 3 – Effect of the doping density of the p -CIGS absorber layer thickness in ITO/GaSe/CIGS on the solar cell electrical parameters.

Concomitantly, an enhancement in V_{oc} improves the solar cell PCE. Additionally, it is worth mentioning the effect of the depletion width W_d and its effect on the

photogenerated current and its impact on the obtained overall cell performance. As previously, the photogenerated current is directly in proportion to depletion width. The W_d is principally affected by the carrier concentration. When the W_d is wider, more carrier collection happens; therefore, more photogenerated current exists, improving the V_{oc} . To further enhance the solar cell performance, a thin film strongly doped p -type is employed (CIGS- p^+) to the structure, *i.e.*, ITO/GaSe/CIGS/CIGS- p^+ . The engagement of the CIGS- p^+ layer was observed to enhance the performance of the solar cell. The simulation was performed using two different absorber thicknesses. For the first case, when both layers, *i.e.*, the CIGS and the CIGS- p^+ , are set to 500 nm. The obtained results are PCE of 31.94%, V_{oc} of 1.159V, J_{sc} of 30.78.41 mA/cm², and FF of 89.46%. Secondly, the CIGS and the CIGS- p^+ thicknesses are set to 1000 nm. For this case, the PCE has increased to 34.09%, revealing V_{oc} of 1.18 V, J_{sc} of 32.27 mA/cm², and FF of 89.61%. The obtained performance values are collected in Table 2. The above results might be discussed and interpreted in light of the recombination processes at the back contact and their direct impact on enhancing the device performance. Many photogenerated carriers are to be expected to undergo the electron-hole recombination process at the back contact, and fewer ones can subscribe to quantum efficiency. Adding CIGS- p^+ leads to more photogenerated carriers than can be collected before the recombination process, and for this reason, the efficiency is enhanced. Interestingly, adding the CIGS- p^+ layer forms a back-surface field (BSF) for the photogenerated electrons [37]. This back-surface field (BSF) acts as a hole transport layer (HTL) at the back contact, which causes a reduction in back-contact recombination, enhancing the overall cell performance. The relationship between the BSF and the recombination rate at the back contact has been studied and explored experimentally [39]. The observed enhancement in the solar cell performance with the layer thickness increase, from 1000 nm to 2000 nm, is because the back contact recombination current density is lowered with a thicker layer since the back contact is located a long way from the depletion region.

Table 2

Solar cell performance comparison between all structures at different absorber layer thicknesses

Structure	Thickness (nm)	V_{oc} (V)	J_{sc} (mA/cm ²)	FF (%)	PCE (%)
GaSe/CIGS	500	0.91	25.20	83.02	19.02
	1000	0.93	28.41	85.12	22.59
GaSe/CIGS/CIGS- p^+	500	1.16	30.78	89.49	31.94
	1000	1.18	32.27	89.61	34.09
GaSe/CIGS/CIGS- p^+ /MoS ₂	333	1.17	29.94	89.59	31.49
	1000	1.19	32.39	89.64	34.55

For additional progression in the solar cell performance, a new novel structure ITO/GaSe/CIGS/CIGS- p^+ /MoS₂ is considered. In this structure, a MoS₂ layer is

added as an interfacial layer between the absorber and the back contact. The obtained results are PCE of 31.49% (34.55%), V_{oc} of 1.16 V (1.19 V), J_{sc} of 29.94 mA/cm² (32.39 mA/cm²), and FF of 89.59% (89.64%) using each layer of thickness of 333 nm (1000 nm), respectively. The obtained results can be understood in terms of the CIGS- p^+ /MoS₂ heterojunction. The insertion of the MoS₂ layer develops the so-called type-II heterojunction [40]. Here it is assumed that the valence band maximum (VBM) and conduction band minimum (CBM) of CIGS- p^+ are less than that of the p -MoS₂ by ~ 0.11 eV and 0.24 eV, respectively. This band alignment helps in the charge separation process as the holes transfer to MoS₂ and electrons transfer to CIGS- p^+ . The formation of the MoS₂ layer between the absorber and Mo back contact mediates the ohmic-contact development rather than the Schottky-type one. Inserting this kind of interfacial layer creates a surface layer with an n -type electrical conductivity characteristic between the absorber and buffer layers. This layer has been called ordered defect (ODC) [41]. This causes an increase of the absorber bandgap at the buffer/absorber interface due to the caused shifting in the VBM to the Fermi level. This reveals a lower interface recombination rate accordingly leading to an enhancement of the solar cell performance.

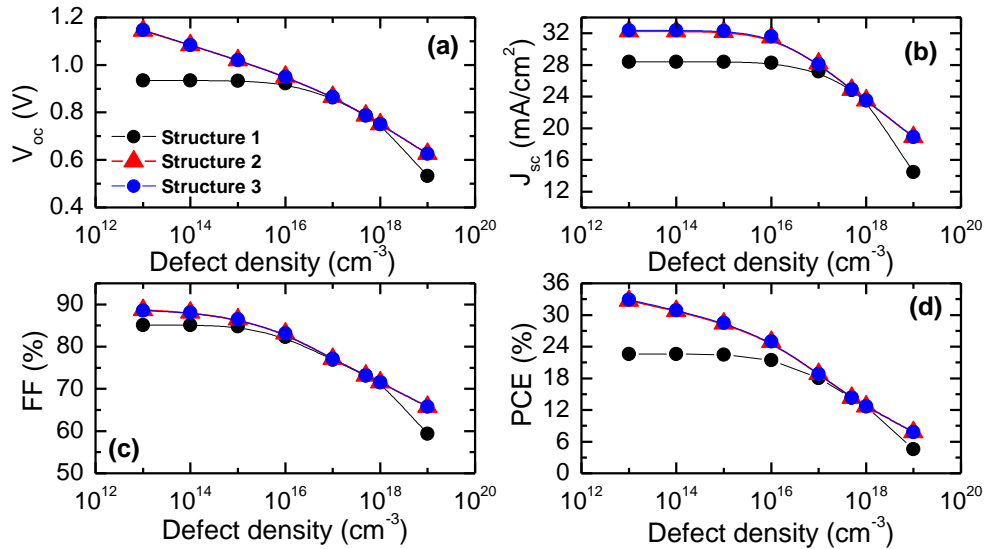


Fig. 4 – (Online Color) The photovoltaic performance parameters of the three structures from 1 to 3 GaSe/CIGS, GaSe/CIGS/CIGS- p^+ , and GaSe/CIGS/CIGS- p^+ /MoS₂, respectively, using GaSe as a buffer layer.

The defect states in bulk materials directly affect the optoelectronic properties of thin film semiconductors. The defects might behave as recombination areas for the photogenerated carriers. Figure 4 discusses the impact of defect densities on the

photovoltaic parameters of the three structures, *i.e.*, GaSe/CIGS, GaSe/CIGS/CIGS-p⁺, and GaSe/CIGS/CIGS-p⁺/MoS₂, respectively. The defect density states for each absorber were varied from 10¹³ cm⁻³ to 10¹⁹ cm⁻³. As observed, Fig. 4 depicts the adverse behavior in the photovoltaic parameters PCE, J_{sc} , FF, and V_{oc} , increasing the defect density level. Namely, the conversion efficiency of structures GaSe/CIGS, GaSe/CIGS/CIGS-p⁺, and GaSe/CIGS/CIGS-p⁺/MoS₂ decreased from 22.59% to 4.58%, from 32.72% to 7.78%, and from 32.9% to 7.5%, with an increase in defect density from 10¹³ cm⁻³ to 10¹⁹ cm⁻³, respectively. Figure 4a shows that increasing the defect density from 10¹³ cm⁻³ to 10¹⁹ cm⁻³ results in a decrease in the V_{oc} . V_{oc} drops from 0.9342 V to 0.533 V, 1.1439 V to 0.626 V, and 1.147 V to 0.788 V, respectively. Indeed, there are no unique clarifications under which conditions defect formation occurs and how it affects the device behavior. Nevertheless, in the CIGS solar cells, previous studies reported that the presence of an In-rich *n*-type material at the surface of the *p*-type CIGS causes large band bending that contributes to the device performance [42]. This layer is called a surface defect layer (SDL), structurally like the bulk CIGS. However, it has different compositional distributions [42, 43]. Moreover, defect states work as trapping locations for photogenerated electron-hole pairs, blocking them from being gathered at both the front and back contacts, increasing the recombination rates and causing a degradation of device performance.

To better understand the abovementioned results, we correlated the results to the rate of saturation of the carrier recombination produced by these defects. The greater the defect density leads to a high level and can cause a change in the band gap structure for all absorbers layers, hurting the absorption process with a significant decrease in the J_{sc} . The effect of the defects on the device performance can be understood as follows. With increasing the defects concentration, defect states are established. These states act as trapping centers for the photogenerated charge carriers, preventing and obstacle them from reaching the back contacts, leading to a pronounced drop in the device performance. Therefore, having high-quality active layers is necessary for future industrial developments. The impact of defects in CZTS has been investigated deeply by Chen *et al.* [44]. They found that the formation energy defects of donors had a higher value than those of acceptors. An additional study by Wang *et al.* [45] revealed that the activation energy of CZTS has a lower value than its bandgap. Consequently, deep defect levels have an enormous impact on recombination loss. As defect levels go deeper, dominant recombination of the photogenerated charge carriers at the layers, interfaces attain. As a result, a reversal performance of the photovoltaic device occurs. This negative impact of defects on the solar cell performance can be ascribed mainly to the decrease in the charge carrier's lifetime and a shortening in the diffusion length between electrons and holes in the absorber layer, which enhance the recombination losses at the interfaces. Figure 5 declares the impact of defect density variations on each absorber's recombination current density. If a *p*-type material with a thickness (d) is

assumed, the excess minority carrier density Δn , is computed *via* recombination current and the effective minority carrier lifetime (τ_{eff}) as below:

$$J_{rec} = \frac{qd\Delta n}{\tau_{eff}} \quad (6)$$

As shown in Fig. 5, the recombination current for the first structure displays a slightly higher value than the other structure. At moderate defect density, the recombination rate is almost constant for all structures up to 10^{16} cm^{-3} . Above a defect density of 10^{16} cm^{-3} , all structures show a sharp linear increase in the recombination current, and at 10^{19} cm^{-3} it is more enhanced for the third structure. Since the defect density has a direct effect on the diffusion length and lifetime of the photogenerated charge carriers, it can be concluded from Fig. 5 that the performance of the photovoltaic devices is impacted directly by the defect density. The pronounced increase in the recombination current at high defect density for all structures is direct evidence of the shortening of the lifetime of the charge carriers and their diffusion length.

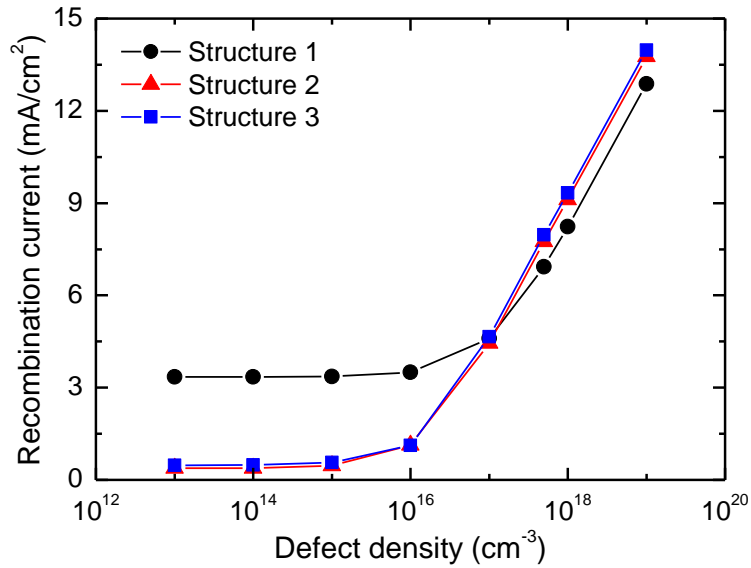


Fig. 5 – (Online Color) The recombination current density as a function of the total defect density for the three structures.

Figure 6 depicts the J - V characteristics and the role of operating temperature on the performance of solar cells. A close look at the photovoltaic parameters at a fixed temperature shows an enhancement of the parameters as moving from structure 1 toward structure 3. The third structure reflects the best performance output. For example, at 300 K, the V_{oc} of ITO/GaSe/CIGS, ITO/GaSe/CIGS/CIGS-p, and

ITO/GaSe/CIGS/CIGS-p⁺/p-MoS₂ are 0.093 V, 1.14 V, and 1.15 V, respectively. As can be observed from Fig. 6, V_{oc} decreases with increasing the operating temperature of all structures. Increasing the temperature causes a reduction in semiconductor bandgap in conjunction with an increase in intrinsic carrier concentration n_i , leading to an increase in reverse saturation current density J_o , hence, an increase in V_{oc} . The solar cell performance is negatively affected when operating at higher temperatures because of the material conductivity. Accordingly, the J_o is affected by the operating temperature according to eq. 7:

$$J_o = AT^3 e^{-(E_{g0}/K_B T)} \quad (7)$$

E_{g0} is the bandgap at null Kelvin. In most general cases, A is a constant of a given material, whereas the bandgap values for semiconductors decrease with an increase in the semiconductor temperature. Figure 7 displays the simulation results at temperatures between 300 K and 500 K. Figure 3a indicates that the V_{oc} decreases with the increase in temperature. For example, for structure 1, the V_{oc} decreases from 0.93 V to 0.52 V by increasing the temperature from 300 to 500 K, respectively. For ITO/GaSe/CIGS/CIGS-p⁺ and ITO/GaSe/CIGS/CIGS-p⁺/p-MoS₂ structures, the V_{oc} falls from 1.14 V to 0.88 V and from 1.15 V to 0.89 V as the temperature increases from 300 K to 500 K, respectively. On the other hand, the J_{sc} is almost constant as the temperature rises to 500 K for all simulated cell structures. Looking at the obtained results, J_{sc} values of 28.41 mA/cm², 32 mA/cm², and 32 mA/cm² have been determined for ITO/GaSe/CIGS/, ITO/GaSe/CIGS/CIGS-p⁺ and ITO/GaSe/CIGS/CIGS-p⁺/p-MoS₂ structures, respectively. Furthermore, FF for all structures decreases with a temperature increase from 300 K to 500 K. For example, the FF of ITO/GaSe/CIGS/CIGS-p⁺/p-MoS₂ decreases from 88.56% to 80.09%, whereas the V_{oc} decreased by 0.4 V within the same temperature range. According to Fig. 4d, the ITO/GaSe/CIGS structure exhibits an optimum PCE of 22.59% at an operating temperature of 300 K. The ITO/GaSe/CIGS/CIGS-p⁺/p-MoS₂ structure were found to be less susceptible to the temperature than any of the other structures. It can be noticed that the PCE values decrease with increasing temperature, as expected. With the increase of the operating temperature to 500 K, PCE values for ITO/GaSe/CIGS, ITO/GaSe/CIGS/CIGS-p⁺, and ITO/GaSe/CIGS/CIGS-p⁺/p-MoS₂ decrease to 10.68% and 22.92%, and 23.11% respectively. The almost linear behavior of the reduction in the V_{oc} and conversion efficiency is discussed as the increase in the darkness current. Additionally, by associating an increase in the temperature, we see a narrowing in the band gap [29]. This feature speeds up an electron and hole recombination between the conduction and valence band and as such increases the dark current in the cell. The performance characteristics of the three investigated solar cells are collected in Table 3. According to the obtained results, the coefficient of voltage variation to temperature $\Delta V_{oc}/\Delta T$ for ITO/GaSe/CIGS, ITO/GaSe/CIGS/ CIGS-p⁺, and ITO/GaSe/CIGS/CIGS-p⁺/p-MoS₂ solar cells, respectively, are given as follows, -2.06 mV/K, -1.3 mV/K, and -1.28 mV/K, respectively.

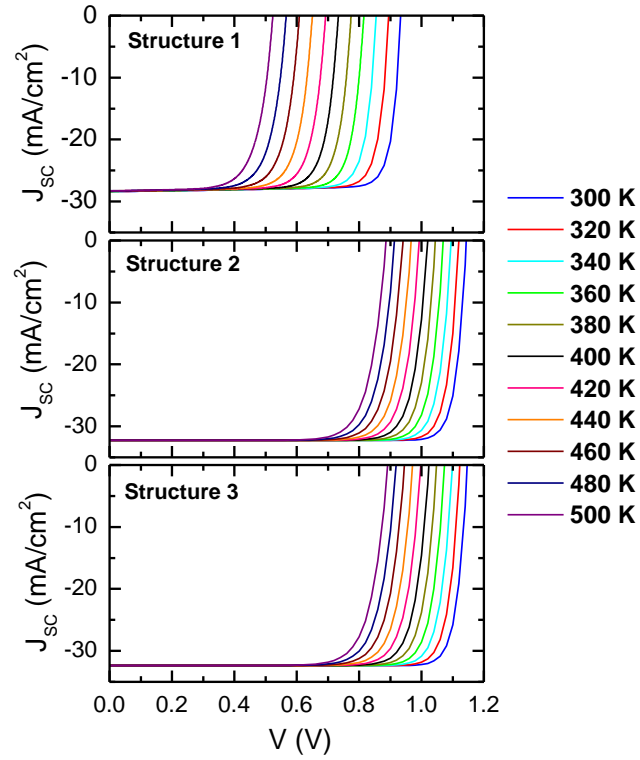


Fig. 6 – (Online Color) The J - V characteristics for the three structures at different temperatures.

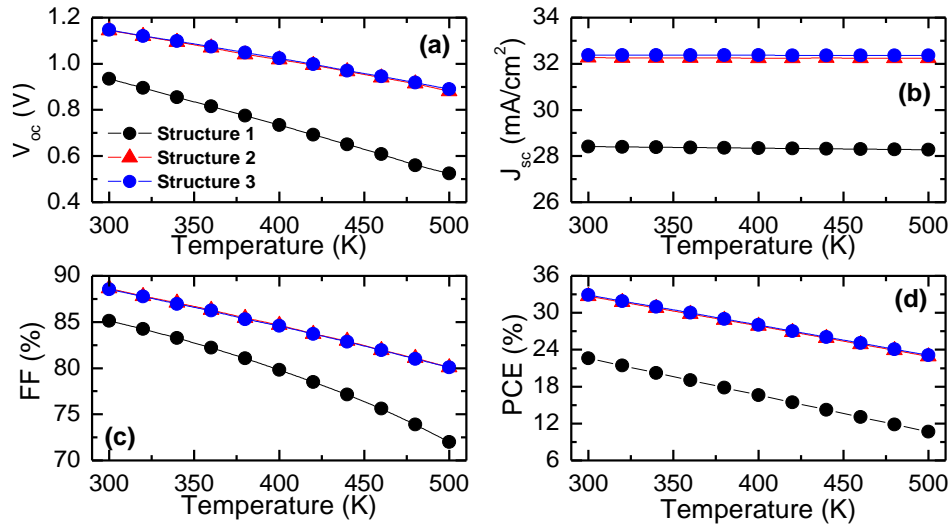


Fig. 7 – (Online Color) The photovoltaic parameters of the solar cells as a function of temperature for the three structures.

Table 3

The obtained performance behavior against the temperature

Parameters	Structure 1	Structure 2	Structure 3
$\Delta V_{oc}/\Delta T$ (mV/K)	-2.060	-1.30	-1.280
$\Delta PCE/\Delta T$ (%/°C)	-0.059	-0.049	-0.048
$\Delta FF/\Delta T$ (%/°C)	-0.065	-0.042	-0.042

4. CONCLUSIONS

This work analyzes a novel heterostructure CIGS-based solar cell using the SCAPS simulation. The CIGS is used as the absorbent layer, GaSe as a buffer layer, and ITO as an OTC layer. The solar cell structures used for this simulation study are ITO/GaSe/CIGS and ITO/GaSe/CIGS/ CIGS- p^+ , and ITO/GaSe/CIGS/ CIGS- p^+ /MoS₂. The engagement of the CIGS- p^+ layer increased the PCE to 31.94%, revealing V_{oc} of 1.159 V, J_{sc} of 30.78.41 mA/cm², and FF of 89.46%. The impact of the p -MoS₂ interfacial layer on CIGS-based thin-film solar cells is analyzed. The results reveal that the formation of the MoS₂ layer between the absorber and Mo back contact improves the overall performance of the device, which mediates the ohmic-contact development. The optimized obtained PCE is 34.55%, with V_{oc} of 1.19 V, J_{sc} of 32.39 mA/cm², and FF of 89.64%. Moreover, all structures were explored with defect state density in the active layer region. The observed loss in the performance in the photovoltaic output parameters is mainly attributed to the increase in the recombination current since the defect states serve as trapping centers for photogenerated electron-hole pairs. An adverse effect on efficiency is observed for all structures with increasing operating temperature. The work uniquely uses GaSe material as a buffer layer with a thin film (CIGS- p^+) with a p -MoS₂ as an interfacial layer to achieve high performance.

Acknowledgments. The authors acknowledge Marc Burgelman for providing the SCAPS-1D software.

REFERENCES

1. A. A. Harry and P. Albert, *Nat. Mater.* **9**, 205–213 (2010).
2. R. N. Bhattacharya, M. A. Contreras, B. Egaas, R. N. Noufi, A. Kanevce, J. R. Sites, *Appl. Phys. Lett.* **89**, 253503 (2006).
3. M. Powalla, P. Jackson, W. Witte, D. Hariskos, S. Paetel, C. Tschamber and W. Wischmann, *Energy Mater. Sol. Cells* **119**, 51 (2013).
4. A. Chirilă *et al.*, *Nature Mater.* **10** (11), 857 (2011).
5. M. Moustafa, T. Al Zoubi, and S. Yasin, *Optical Materials* **124**, 112001 (2022).
6. M. Asaduzzaman, M. Hasan, A. N. Bahar, *Springerplus* **5**, 578 (2016).

7. M. Bar, W. Bohne, J. Rohrich, E. Strub, S. Lindner, M. C. Lux-Steiner, C. H. Fischer, T. P. Niesen, F. Karg, *J. Appl. Phys.* **96**, 3857–3860 (2004).
8. B. Peace, J. Claypoole, N. Sun, D. Dwyer, M. D. Eisaman, P. Haldar, H. Efstathiadis, *J. Alloys Compd.* **657**, 873–877 (2016).
9. P. Jackson, D. Hariskos, E. Lotter, S. Paetel, R. Wuerz, R. Menner, W. Wischmann, M. Powalla, *Prog. Photovoltaics Res. Appl.* **19**, 894–897 (2011).
10. E. Wallin, U. Malm, T. Jarmar, O. Edoff, and L. Stolt, *Prog. Photovolt., Res. Appl.* **20** (7), 851 (2012).
11. I. Repins *et al.*, *Photovoltaics Res. Appl.* **16** (3), 235 (2008).
12. C. Platzer-Bjorkman, T. Torndahl, D. Abou-Ras, J. Malmstrom, J. Kessler, L. Stolt, *J. Appl. Phys.* **100**, 044506 (2006).
13. M. Moradi, R. Teimouri, M. Saadat, M. Zahedifar, *Optik* **136**, 222–227 (2017).
14. B. Sara, Z. Baya, B. Zineb, *Materials Science-Poland* **36**(3), 514–519 (2018).
15. Md. Billal Hosen, Md. Karamot Ali, Ali Newaz Bahar, *International Journal of Photoenergy* **2017**, 4561208 (2017).
16. K. S. Gour, R. Parmar, R. Kumar, V. N Singh, *J. Nanosci. Nanotechnol.* **20**(6), 3622–3635 (2020).
17. A. Seyhan, O. Karabulut, B.G Akmoğlu, B. Aslan, R. Turan, *Cryst. Res. Technol.* **409**, 893–895 (2005).
18. M. M. Abdullah, G. Bhagavannarayana, M. A. Wahab, *J. Mater. Sci.* **45**, 4088–4092 (2010).
19. A. Ashkhasi, B. Gürbulak, M. Sata, G. Turgut, S. Duman, *AIP Conf. Proc.* **1815** (2017).
20. Le Toullec, M. Balkanski, J. M. Besson, A. Kuhn, *Phys. Lett. A* **55**, 245–246 (1975).
21. Y. Fan, T. Schittkowski, M. Bauer, L. Kador, K. R. Allakhverdiev, E. Y. Salaev, *J. Lumin.* **98**, 7–13 (2002).
22. K. Orgassa, H. W. Schock, J. H. Werner, *Thin Solid Films* 431–432, 387 (2003).
23. R. J. Matson, O. Jamjoum, A. D. Buonaquist, P. E. Russell, L. L. Kazmerski, P. Sheldon, R.K. Ahrenkiel, *Sol. Cells* **11**, 301(1984).
24. P. E. Russell, O. Jamjoum, R. K. Ahrenkiel, L. L. Kazmerski, R. A. Mickelsen, W. S. Chen, *Appl. Phys. Lett.* **40** (11), 995 (1982).
25. T. Wada, N. Kohara, S. Nishiwaki, T. Negami, *Thin Solid Films* **387**, 118–122 (2001).
26. S. Nishiwaki, N. Kohara, T. Negami, M. Nishitani, T. Wada, *Jpn. J. Appl. Phys.* **37** L71–L73 (1998).
27. W. N. Shafarman, J. E. Phillips, in: *Proceedings of the 25th IEEE Photovoltaic Specialists Conference*, Washington D.C., USA, May 13–17, 1996, p. 917.
28. Th. Böker, R. Severin, A. Müller, C. Janowitz, and R. Manzke, D. Voss, P. Krüger, A. Mazur, and J. Pollmann, *Phys. Rev. B* **64**, 235305 (2001).
29. P. Singh, S. N. Singh, M. Lal, M. Husain, *Solar Energy Materials and Solar Cells* **92**(12), 1611–1616 (2008).
30. M. Burgelman, K. Decock, S. Khelifi, A. Abass, *Thin Solid Films* **535**, 296–301 (2013).
31. M. Burgelman, P. Nollet, S. Degrave, *Thin Solid Films* **361-362**, 527–532 (2000).
32. M. Moustafa, T. Alzoubi, *Mod. Phys. Lett. B.* **32**, 1850269 (2018).
33. M. Moustafa, T. AlZoubi, *Optik* **170**, 101–105 (2018).
34. S. Yasin, T. Al Zoubi, M. Moustafa, *Optik* **229**, 166258 (2021).
35. T. Alzoubi, M. Moustafa, *Mod. Phys. Lett. B.* **34**, 2050065 (2020).
36. K. Jiao, C. Duan, X. Wu, J. Chen, Y. Wang, Y. Chen, *Phys. Chem. Chem. Phys.* **17**, 8182–8186 (2015).
37. M. Mostefaoui, H. Mazari, S. Khelifi, A. Bouraiou and R. Dabou, *Energy Procedia* **74**, 736–744 (2015).
38. S. Ouédraogo, F. Zougmoré, J. Ndjaka, *Int. J. Photoenergy* **2013**, 1–9 (2013).
39. A. Patel, P. Kumar Rao, R. Mishra, S. Kumar Soni, *Optik* **243**, 167498 (2021).

40. D. Gross, I. Mora-Seró, T. Dittrich, A. Belaidi, C. Mauser, A. J. Houtepen, E. D. Como, A. L. Rogach, J. Feldmann, *J. Am. Chem. Soc.* **132**, 5981–5983 (2010).
41. I. M. Dharmadasa, J. D. Bunning, A.P. Samantilleke, T. Shen, *Sol. Energy Mater. Sol. Cells.* **86**, 373–384 (2005).
42. Y. Yan, K.M. Jones, J. Abushama, M. Young, S. Asher, M.M. Al-Jassim, R. Noufi, *Appl. Phys. Lett.* **81**, 1008 (2002).
43. Z. Li, X. Yu-Ming, X. Chuan-Ming, H. Qing, L. F. Fang, L. Chang-Jian, S. Yun, *Thin Solid Films* **520**, 2873(2012).
44. S. Chen, J.-H. Yang, X.G. Gong, A. Walsh, S.-H. Wei, *Phys. Rev. B* **81**, 245204 (2010).
45. K. Wang, B. Shin, K.B. Reuter, T. Todorov, D.B. Mitzi, S. Guha, *Appl. Phys. Lett.* **98**, 051912 (2011).